

Portable Food-Freshness Prediction Platform Based on Colorimetric Barcode Combinatorics and Deep Convolutional Neural Networks

Lingling Guo, Ting Wang, Zhonghua Wu, Jianwu Wang, Ming Wang, Zequn Cui, Shaobo Ji, Jianfei Cai,* Chuanlai Xu,* and Xiaodong Chen*

Artificial scent screening systems (known as electronic noses, E-noses) have been researched extensively. A portable, automatic, and accurate, real-time E-nose requires both robust cross-reactive sensing and fingerprint pattern recognition. Few E-noses have been commercialized because they suffer from either sensing or pattern-recognition issues. Here, cross-reactive colorimetric barcode combinatorics and deep convolutional neural networks (DCNNs) are combined to form a system for monitoring meat freshness that concurrently provides scent fingerprint and fingerprint recognition. The barcodes—comprising 20 different types of porous nanocomposites of chitosan, dye, and cellulose acetate—form scent fingerprints that are identifiable by DCNN. A fully supervised DCNN trained using 3475 labeled barcode images predicts meat freshness with an overall accuracy of 98.5%. Incorporating DCNN into a smartphone application forms a simple platform for rapid barcode scanning and identification of food freshness in real time. The system is fast, accurate, and non-destructive, enabling consumers and all stakeholders in the food supply chain to monitor food freshness.

The mammalian olfactory system can accurately discriminate trillions of scents despite having only hundreds of olfactory receptors.^[1] These receptors have an affinity for a range of scent molecules. One scent molecule may bind to different receptors with varying affinities and activate several receptors at once, forming a complex scent fingerprint^[2,3] that is carried to the central nervous system (CNS) for analysis (Figure 1a).^[4–6] It is this integration of olfactory receptor combinatorics with CNS pattern recognition that allows the olfactory system to discriminate scents so efficiently.

Mimicking the olfactory system for accurate, portable and real-time artificial scent screening requires two crucial and inseparable components: cross-reactive sensing and fingerprint pattern recognition.^[7–9] Inspired by nature, artificial scent screening systems resembling the mammalian system (known as E-noses, opto-

noses for olfactory, and E-tongue for taste) have been developed for disease diagnosis^[10] and detection of environmental contaminants,^[11,12] explosives,^[13] food, and drugs.^[14–17] Cross-reactive sensing in these artificial systems is achieved using cross-reactive metal oxide^[18,19] or colorimetric sensor arrays^[20–23] that interact differentially with target molecules to generate a fingerprint pattern. Traditional statistical methods such as linear discriminant analysis (LDA), principal component analysis (PCA) and hierarchical cluster analysis (HCA) are typically used to analyze the fingerprints.^[8,24]


While e-noses have been extensively researched, few have been commercialized because they suffer from either sensing or pattern-recognition issues. For example, metal oxide-based E-noses generally require high temperatures to function and depend on cumbersome power supply and wiring.^[25] Furthermore, these sensors are sensitive to humidity and cannot distinguish closely similar compounds.^[24] While colorimetric sensors (or opto-noses) are highly cross-reactive and perform well at room temperature, they produce 3^n (where 3 represents red, green, blue (RGB) and n is number of sensors) non-linear, multidimensional datasets that cannot be accurately extracted and analyzed using statistical methods such as PCA, LDA, or HCA.^[24,26] To commercialize E-noses, we need a system that

Dr. L. Guo, Prof. C. Xu
International Joint Research Laboratory for Biointerface and Biodetection
State Key Lab of Food Science and Technology, and School of Food
Science and Technology
Jiangnan University
1800 Lihu Road, Wuxi, Jiangsu Province 214122, P. R. China
E-mail: xcl@jiangnan.edu.cn

Dr. T. Wang, Dr. J. Wang, Dr. M. Wang, Dr. Z. Cui, Dr. S. Ji, Prof. X. Chen
Innovative Center for Flexible Devices (iFLEX)
Max Planck–NTU Joint Lab for Artificial Senses
School of Materials Science and Engineering
Nanyang Technological University
50 Nanyang Avenue, Singapore 639798, Singapore
E-mail: chenxd@ntu.edu.sg

Z. Wu
School of Computer Science and Engineering
Nanyang Technological University
50 Nanyang Avenue, Singapore 639798, Singapore

Prof. J. Cai
Department of Data Science & AI
Monash University
Clayton, Victoria 3168, Australia
E-mail: Jianfei.Cai@monash.edu

 The ORCID identification number(s) for the author(s) of this article can be found under <https://doi.org/10.1002/adma.202004805>.

DOI: 10.1002/adma.202004805

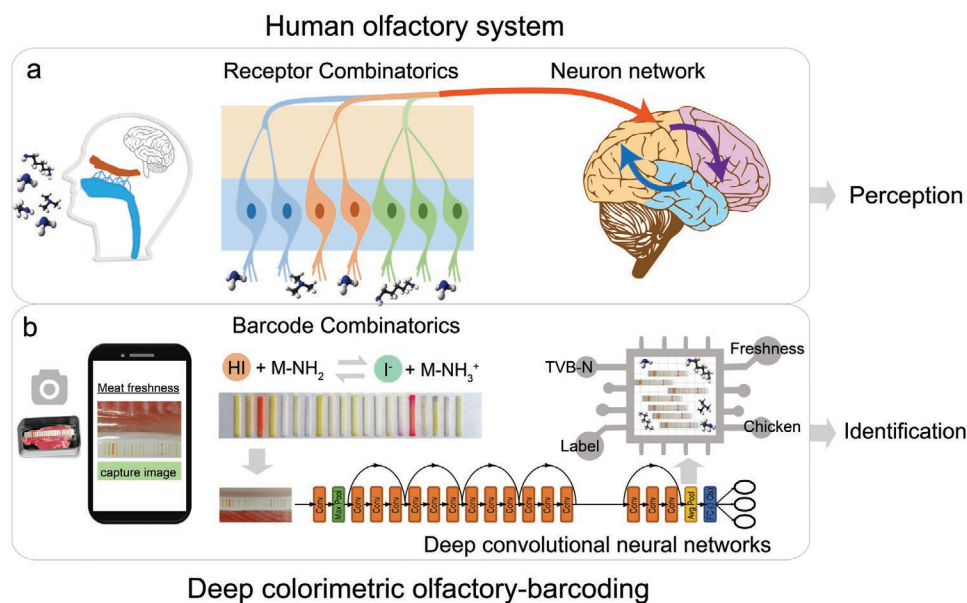


Figure 1. Working principle of the human olfactory system and our system based on colorimetric barcode combinatorics and DCNN. a) In the human olfactory system, volatile amines from meat activate several odor-binding proteins of the olfactory cell (left) and trigger electrochemical potentials that travel to the brain center via olfactory nerve fibers (middle). Tapping on prior knowledge, the brain analyses the action potential patterns and identifies them as different levels of meat freshness (right). b) In our system, volatile amines from meat interact with sensors in the barcode and trigger a color change according to the principle of halochromism. Colorimetric barcode image showing barcode combinatorics is captured and wirelessly uploaded to the cloud via a smartphone APP. Using a trained DCNN, meat freshness can be displayed on the smartphone within 30 s.

has both a robust cross-reactive sensor array and a data analysis method that can extract information from non-linear datasets and accurately predict fingerprint patterns.

Here, we integrated colorimetric barcode combinatorics with deep convolutional neural networks (DCNNs) to form a system that concurrently provides scent fingerprint and intelligent fingerprint recognition (Figure 1b). We used the system, which we call deep colorimetric olfactory-barcoding, to automatically screen the freshness of different types of meats. The colorimetric barcode is made up of 20 different types of porous nanocomposite comprised of dye-loaded chitosan nanoparticles (CNP-dye) embedded on cellulose acetate (CA). The halochromic dyes in the barcode cross-react according to the type and concentration of gases to form a scent fingerprint (in the form of a colorful barcode) that is identified using DCNN. Using fully supervised training techniques and 3475 labeled barcode images as the training source, we obtained a DCNN that predicted meat freshness with an overall accuracy of 98.5%. Incorporating DCNN into the smartphone software enables a user to identify the freshness of meats within 30 s by simply scanning the barcode. Our system is fast, automated, accurate and non-destructive. Because our system uses common biodegradable and biocompatible materials, and was studied under typical food packaging conditions, it is applicable everywhere along the food supply chain for real-time monitoring of food freshness.

To make the colorimetric strips, we patterned the gas sensitive barcodes on poly(dimethylsiloxane) (PDMS)—a chemically inert, moisture-resistant and transparent substrate. The barcode is made of porous nanocomposites comprising of dye-containing chitosan nanoparticles (CNP-Dye) embedded in a CA matrix (CNP-Dye/CA) (Figure 2a). The CNP-Dye were

prepared according to the ionic gelation method using sodium tripolyphosphate as the cross-linker.^[27] Both chitosan and CA are biodegradable and non-toxic, making them biocompatible and environmentally friendly options for screening food freshness.^[28,29] To realize cross-reactivity between the bars of the barcode in the same way human olfactory receptors cross-react, we created 20 different CNP-Dye/CA solutions, one for each bar of the barcode. Each CNP-Dye/CA solution contained a different type of halochromic dye whose chromophore changes color according to the surrounding pH (Table S1, Supporting Information).^[30] Each of the 20 different dyes responds within a different pH range, covering the detection range of gases emitted from rotting meats. With the spoilage of meat, the concentration of bioamines in the sealed package increases due to microorganism-induced protein degradation and gas accumulation effect. Take bromothymol blue (BPB, the first strip) as an example, the basic bioamines leads to a splitting of the hydroxyl group of acid BPB (Figure S1, Supporting Information), which results in a visible color change from yellow (protonated form) to blue (deprotonated form). When exposed to different gases with varying concentrations, each bar of the barcode will display a different color or range of coloration. This colorful barcode forms the gas fingerprint.

To deposit the gas sensitive barcodes on PDMS, we created hydrophilic barcode patterns on PDMS with thickness of 2 mm using a shadow mask and oxygen plasma processing (30%, 2 min) (Figure 2b). Drop-casting each of the twenty CNP-Dye/CA solutions onto each successive bar within 10 min forms the colorimetric barcode. Each bar is 1 mm long and 0.6 mm wide; the gap between the neighboring bar is 1 mm.

Gas transfer and sensing stability depend on the microstructure of the nanocomposites and their ability to preserve the

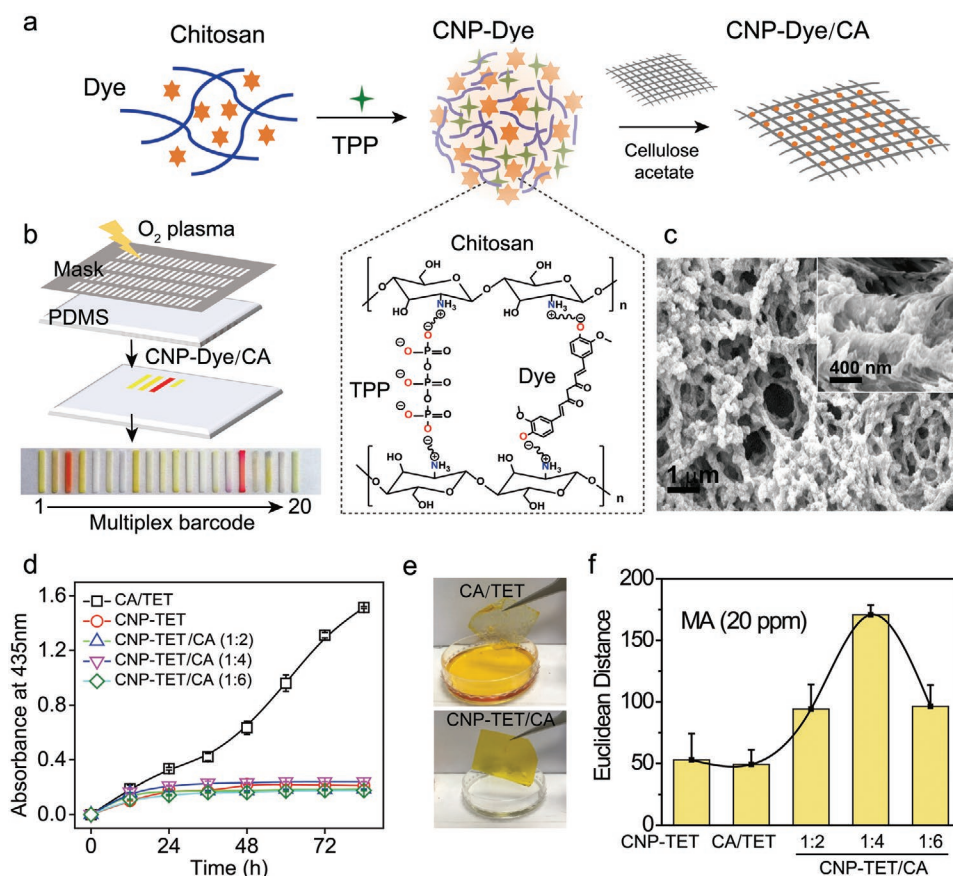


Figure 2. Fabrication and characterization of colorimetric barcode strips. a) Schematic showing the fabrication of CNP-Dye/CA. Dyes (orange stars) are cross-linked with chitosan (blue lines) using sodium tripolyphosphate (TPP, green star) according to the ionic gelation method. CNP-Dye is embedded on cellulose acetate (CA) matrix to form CNP-Dye/CA. Inset: chemical structure of one example CNP-Dye. The dye is tetraiodophenolsulfonephthalein (TET). Strong intramolecular forces between positively charged protonated amine groups ($-\text{NH}_3^+$, blue) of chitosan and negatively charged deprotonated hydroxyl groups ($-\text{O}^-$, red) in the dye prevent dye leakage. b) Schematic of barcode patterning on PDMS. Oxygen plasma processing (30%, 2 min) using a shadow mask forms hydrophilic patterns on PDMS. Drop-casting of CNP-Dye/CA solution (1 μL) on the plasma-treated patterns forms the 20-bar colorimetric barcode. Each bar received a different CNP-Dye/CA solution. Barcode size is 1 \times 0.6 mm and gap between neighboring bar is 1 mm. c) Scanning electron microscopy image of CNP-Dye/CA showing the composite is highly porous. The inset shows CNP were immobilized on the surface of CA fibers. d) Dye leakage test for different films show CNP-TET and CNP-TET/CA films had negligible dye leakage. Films were soaked in water for different durations and absorbance of the supernatant were measured at 435 nm. Data are representative of three independent experiments. The error bars are the standard deviation from three independent experiments. e) Photographs of CA/TET and CNP-TET/CA (1:4) films soaked in water for 84 h. Dye leaked from CA/TET but not CNP-TET/CA film. f) Sensing performance of different colorimetric strips exposed to 20 ppm methylamine (MA) gas. Strip response is described by measuring Euclidean distance (ED) of RGB values of the barcode before and after exposure to MA. Curve linking the ED values of different strips is for guiding the eye. Optimal sensing materials of CNP-dye/CA (1:4) was selected for barcode preparation. The error bars are the standard deviation of three independent experiments.

dye. Scanning electron microscopy imaging showed that while CNP-Dye themselves formed aggregates (Figure S2, Supporting Information), they were well distributed on the interweaved fibers that form the porous 3D structure of the CNP-Dye/CA (Figure 2c). Such a porous 3D structure is expected to provide abundant gas sensing sites. We performed a dye leakage experiment by immersing films of CNP-Dye and CNP-Dye/CA in water and characterizing the absorbance of the supernatant. Tetraiodophenolsulfonephthalein (TET) with characteristic absorbance at 435 nm was used as a model dye. For films of TET-containing chitosan nanoparticles (CNP-TET) and CNP-TET embedded in CA (CNP-TET/CA), the supernatant had negligible absorbance at 435 nm and no visible color (Figure 2d,e). In contrast, the supernatant for a film of TET embedded in CA

(CA/TET) was yellow; when immersion time increased from 0 to 84 h at room temperature, the peak intensity at 435 nm increased gradually from 0 to 1.51. These results show that strong intramolecular forces between negatively charged deprotonated hydroxyl groups ($-\text{O}^-$) of TET and positively charged protonated amine groups ($-\text{NH}_3^+$) of chitosan prevented TET from leaking out of the porous composite (inset in Figure 2a). Weak Van der Waals forces between CA and TET in the CA/TET film led to large dye leakage. The strong interaction in CNP-TET/CA that avoids dye leakage ensures the safety of barcode in food packaging.

To test and optimize the sensing performance of our colorimetric barcode, we exposed the strip to methylamine (MA) gas. Increasing concentrations of MA gas turned the barcode

on the strip from yellow to deep blue (Figure S3, Supporting Information). We quantitatively described the barcode response by measuring the Euclidean distance (ED) of the RGB values of the barcode before and after exposure to MA. Exposure to higher concentrations of MA increased the ED value, indicating that MA activated the chromophore and the barcode functioned as a scent sensor (Figure S4, Supporting Information). All the CNP-TET/CA barcodes (formed with different mass ratio of CNP-TET:CA) showed a higher response than both CNPs-TET and CA-TET. We attribute this enhanced performance to the 3D porous structure of CNPs-TET/CA, which facilitates gas transfer and provides more sensing sites. Based on the performance of the different barcodes shown in Figure 2f, we chose the optimal mass ratio of 1:4 for all subsequent experiments.

Proteins in rotting meats are microbially decomposed into peptides and amino acids. Over time, these components are further broken down into low-grade amines and ammonia (NH_3),^[31,32] which are useful freshness indicators. To assess whether our colorimetric barcode strip can be used to monitor meat freshness, we tested the response of the strip to multiple gases typically detected from rotting meats, including ammonia (NH_3), MA, trimethylamine (TMA), putrescine (PUT) and cadaverine (CAD). Like mammalian olfactory receptors where one scent molecule can bind to different receptors and each receptor responds to a range of scents to form a complex scent fingerprint, one type of gas can trigger several bars of our barcode and each bar responds to several gases to form a colorful

combination of bars that represent the fingerprint for these 5 amine gases. Figure 3a shows the colorimetric barcode obtained using a scanner (Canon, LBP7010C, 600 dpi) after exposure to different concentrations of individual amine gases (Figure S5, Supporting Information for RGB images).

We processed the data using traditional ED value, PCA, and HCA methods. EDs of R, G, and B values for each bar of the barcode before and after exposure to the amine gases were calculated. The estimated limit of detection (LOD) for NH_3 , MA, TMA, PUT and CAD were below 50 ppb at signal to noise ratio of 3 (Table S2, Supporting Information). Corresponding to color changes seen in the barcode, higher concentrations of amine gases displayed higher ED values. ED values of our colorimetric barcode quantitatively describe the concentration of the gases. In Figure 3b, ED values have overlaps under 20 ppm, and separate from each other above 20 ppm. Thus, we investigated the ED value for different gases before and after exposure to 20 ppm of the gas. Each gas displayed a distinctive ED value ($n = 8$, $*p < 0.001$), demonstrating that NH_3 , MA, TMA, PUT, and CAD have specific gas fingerprints at 20 ppm (Figure 3c). The reason is that different chemical environments and the number of amino ($-\text{NH}_2$) groups in these five amine gases would induce different color combinations in the barcode.

We further used PCA and HCA—two widely used classification methods^[24]—to evaluate a 50×60 (5 amine gases \times 10 concentration \times 60 RGB values) dimensional matrix acquired from the colorimetric barcode. The gas concentrations

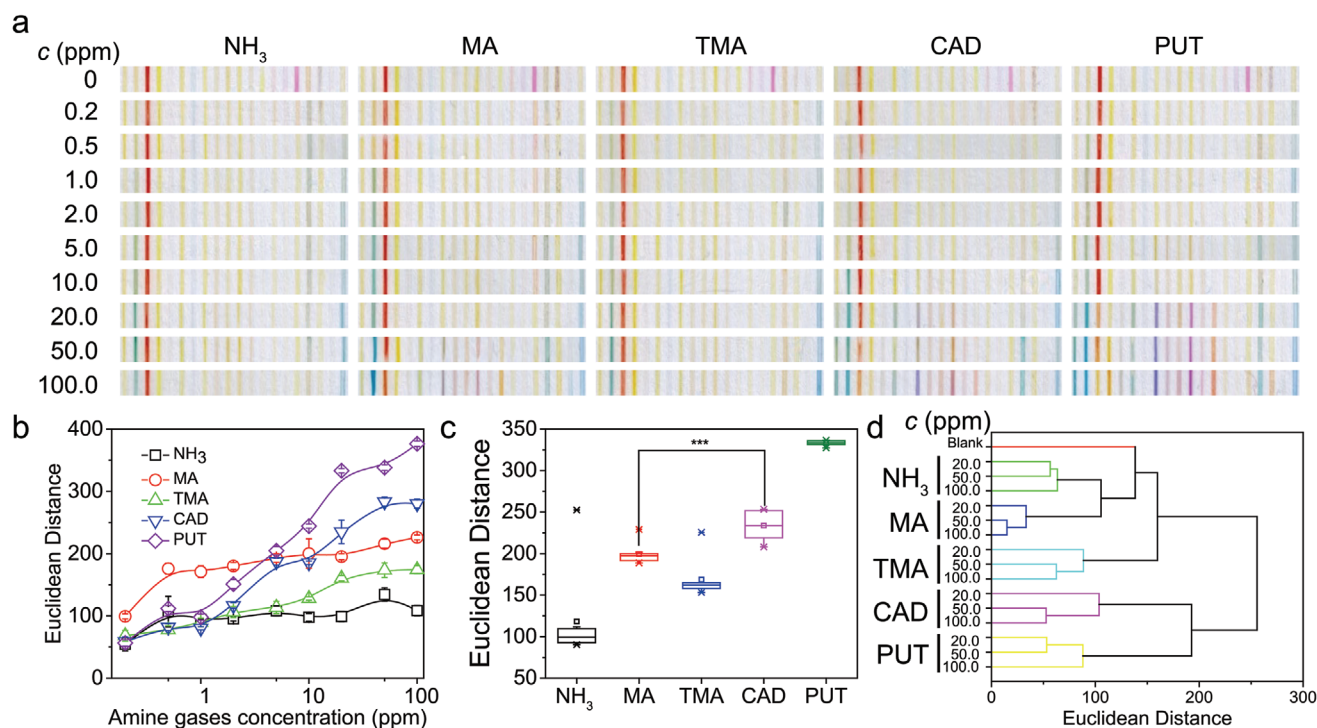


Figure 3. Discrimination of five types of amines gases using colorimetric barcode and traditional statistical methods. a) Scanned images (Canon scanner, LBP7010C, 600 dpi) of barcode exposed to NH_3 , MA, TMA, CAD and PUT show different gases display different bar combinatorics. Barcode color changes as gas concentration increased from 0.20 to 100.0 ppm. b) Euclidean distance of R, G, and B values in the different barcodes increase after exposure to higher concentrations of amine gas. The error bars are the standard deviation from eight independent experiments. c) Boxplot of the distribution of ED values for NH_3 , MA, TMA, CAD, and PUT at 20 ppm ($n = 8$) shows these five amine gases can be clearly distinguished at 20 ppm. *** represents $p < 0.001$ (t-test). d) Cluster tree produced by hierarchical cluster analysis show the five amine gases can be distinguished between 20 and 100 ppm.

examined were between 20 and 100 ppm. PCA creates several independent PCs that maximally represent the whole matrix. From the PCA scree plot, we can see that 6 PCs are required to account for 90% of the total variance, 8 PCs for 95%, and 10 PCs for 99% (Figure S6, Supporting Information). The 3D score plot of PCA using the first three PCs (76.9% of the total variance) shows that clusters of 5 amine gases are clearly separated (Figure S7, Supporting Information).

With HCA, Ward's minimum variance method was used to determine gas-induced variations of the 60 dimensional RGB colorimetric barcode. The generated cluster-tree showed the 5 amine gases formed clearly separate clusters between 20 ppm and 100 ppm (Figure 3d). The PCA score plot and HCA cluster tree both intuitively reveal that our barcode can effectively discriminate NH₃, MA, TMA, CAD, and PUT based on a combination of cross-reactive colorimetric sensors. Together, these results demonstrate that it is possible to use our colorimetric barcode to monitor meat freshness and other microbial metabolic processes in fermented foods such as wine, vinegar and cheese that are known to release CAD and PUT.^[31]

As a proof-of-concept, we used our colorimetric barcode to monitor the freshness of three types of meat—chicken, fish, and beef. To predict meat freshness accurately, we used DCNN to process and recognize the complex multi-dimensional scent fingerprint data. DCNN architecture, which is an end-to-end network with several nonlinear activation functions,^[33–35] is suitable for non-linear multidimension data analysis.^[36–39]

The colorimetric barcodes were glued on and faced toward widely used transparent poly(vinyl chloride) (PVC) meat packaging films without touching meat samples (Figure S8, Supporting Information). Because the barcode is flexible and transparent, it integrates easily with existing polystyrene and PVC packaging materials. The meat packages were stored at 25 °C, and images of the barcode were taken at different time intervals using a smartphone camera without opening the package (Figure S9, Supporting Information). To classify the barcodes into different categories of freshness, we measured the total volatile basic nitrogen (TVB-N) value of the meats using the Conway dish method^[40] an international standard for determining meat freshness (Figure S10, Supporting Information). Here, in order not to inference with the barcode image collection we prepare other packages of meat with the same procedures for TVB-N testing. Meat with TVB-N value ≤15 mg/100 g is considered fresh, 15–20 mg/100 g is cooking edible but less fresh, and ≥20 mg/100 g indicates inedible and spoiled.^[41–43] Then these images were classified according to these three standard categories of freshness—fresh, less fresh, and spoiled. As there are variations of TVB-N threshold for meat with different types and sources, a detailed investigation of TVB-N values of a specific meat is suggested to ensure the accurate classification.

A total of 4161 images of meat and barcode for the three kinds of meat were obtained, forming the dataset for DCNN evaluation of meat freshness. The 4161 images were randomly divided into 3475 images for model training and 686 images for testing (Figure 4a). We designed a three-class image classification network using the ResNet 101 backbone^[44] comprising of input, multiple convolution (conv.), full connection (FC), and output layers. This trained convolutional neural network extracts features of the barcode from the images and classifies

the barcodes into one of the three categories of freshness. As epochs (number of passes the algorithm completes through the entire dataset) increase, the loss that represents the difference between predicted and actual result approaches 0 and the training accuracy improves (Figure 4b).

After training, we used the 686 test images from the dataset to evaluate how accurately DCNN classifies the barcode images. When a barcode image is input into the classification network, the freshness category that the meat most likely belongs to is given (red circles in Figure 4a). For the three kinds of meat, the images were classified with 100% accuracy for the spoiled category; in chicken, accuracy was 99.0% for fresh, 96.3% for less fresh; in fish, accuracy was 98.1% for fresh, 98.8% for less fresh; in beef, accuracy was 95.9% for fresh, 98.8% for less fresh (Figure 4c and Table S3, Supporting Information). The confusion matrix for the 686 images (Figure 4d) and subconfusion matrices for chicken, fish and beef (Figure S11, Supporting Information) whose diagonal show the number of correctly classified samples further illustrate the classification accuracy. DCNN classification reached an overall accuracy of 98.5%.

For comparison, we used ED values to predict meat freshness. To obtain a reference curve, we measured the TVB-N values and calculated the ED values of eight samples for each type of meat stored at different time intervals (0 to 48 h) (Figure S12, Supporting Information). Before calculating the ED values, we corrected for light effects in the images using the center of the colorimetric barcode as a reference point for white balance—the process of removing unrealistic color casts in images. Both TVB-N values of the samples and ED values of the colorimetric barcodes increased when meat storage intervals increased (Figure S12, Supporting Information). Based on the TVB-N values, the meat samples were categorized as fresh, less fresh, and spoiled. The range of ED values corresponding to each category of freshness was accordingly, which was used for prediction of the freshness of an unknown meat sample.

We randomly selected twenty colorimetric barcode images for each freshness category to assess the prediction accuracy of ED. In chicken, ED values achieved prediction accuracy of 35.0% for fresh, 55.0% for less fresh, and 100.0% for spoiled; in fish, it achieved 90.0% for fresh, 30.0% for less fresh, 90.0% for spoiled, and in beef it was 40.0% for fresh, 35.0% for less fresh, 100.0% for spoiled (Figure 4c). ED analysis showed an overall accuracy rate of 61.7%, which is far lower than DCNN classification (98.5%); fresh and less fresh groups had the poorest accuracy rates. We also found that ED values between fresh and less fresh groups for chicken, fish, and beef samples were all not significantly different ($p > 0.05$, Figure S13, Supporting Information), indicating that it is difficult to distinguish fresh from less fresh using ED values. This low prediction accuracy and discrimination efficiency are because ED values are affected by photo shooting conditions such as angle, zoom and lighting. In contrast, the model training processes in DCNN exclude most of these effects. Furthermore, because the RGB values of the barcode do not change linearly with the concentration of the target analyte, using the non-linear DCNN method for data processing is more suitable in this case. To automate the overall screening procedure, we incorporated DCNN in a smartphone application (APP), NTUFoodCheck. The APP provides a user-friendly interface for image collection, image uploading,

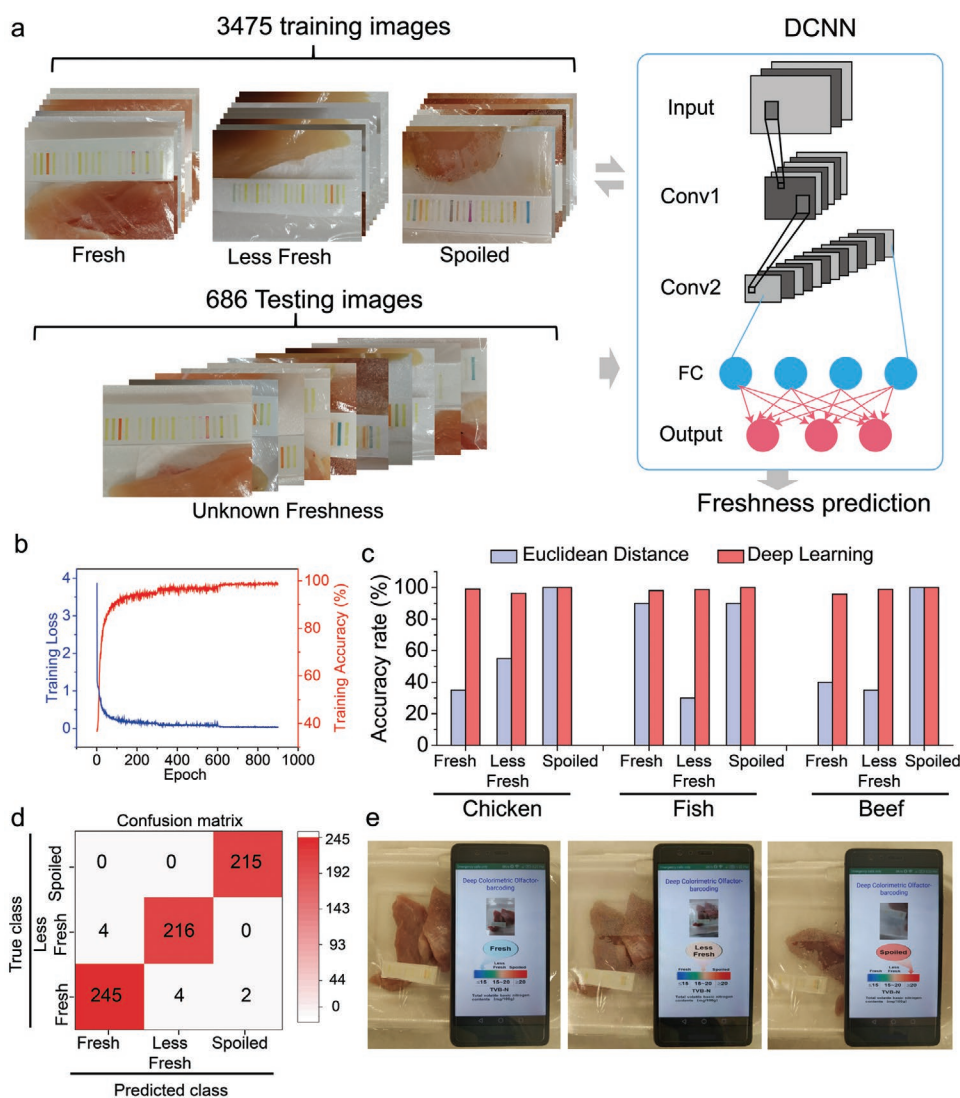


Figure 4. Colorimetric barcode integrated with DCNN as a simple, portable platform for accurate real time monitoring of meat freshness. a) DCNN for barcode recognition. The dataset contained 3475 images for DCNN training and 686 images for model testing (left). DCNN based on the ResNet 101 backbone was used for food freshness classification (right). The DCNN architecture has input, multiple convolution (conv.), full connection (FC) (blue circles), and output layers. When the barcode image is input into the network, the predicted freshness category (red circles) for the test sample is given. b) Training accuracy of DCNN increases as epochs (number of passes the algorithm completes through the entire dataset) increase. Training loss represents the difference between predicted and actual result. c) Comparison of detection accuracy rate for chicken, fish, and beef freshness based on Euclidean distance calculations and DCNN training. DCNN had an overall higher accuracy rate (98.5%) than ED (61.7%). d) Confusion matrix for the 686 test images showing DCNN accurately classified the images into the three freshness categories. Only ten images were wrongly classified. e) Photographs showing smartphone interfaces displaying the state of the meat as either fresh (right panel), less fresh (middle panel), or spoiled (right panel) after scanning the barcode.

and real-time display of the results (Figure 4e). Users simply need to capture the colorimetric barcode image within the APP and meat freshness computed by DCNN will be displayed on the screen within 30 s (Movies S1–S3, Supporting Information). For further validate the applicability of our system in practical refrigeration situations, we integrated our colorimetric barcode in fish package that were stored at 4 °C. 112 images (eight sensors × two photos for each sensor × seven time points) were collected at storage interval from 0 to 5 days and then uploaded in the system for freshness prediction (Figure S14, Supporting Information). Based on TVB-N values as the true freshness

indicator (Figure S15, Supporting Information), we obtained the overall prediction accuracy of 92.0%.

The designed APP can be downloadable onto any smartphone or portable devices; thus our system can be used by both consumers and food suppliers to screen and/or monitor meat freshness in real-time. The issue regarding barcode image difference caused by camera setting could be solved by embedding domain adaptation in the pipeline of deep learning. In case of no cameras available, human can also roughly distinguish different freshness stage based on reference pictures (Figure S9, Supporting Information).

Compared with previous food monitoring researches,^[14,45–53] the barcode system shows good compatibility with food supply chains (details given in Table S4, Supporting Information). On the one hand, our colorimetric barcode with flexibility and editable size could be fully integrated with many packaging materials and techniques. On the other hand, colorimetric barcode recognition can be conducted in a short time (30 s) without bulky wiring, which is compatible with fast food supply chains. Moreover, our system was tested in real application scenarios by using meat packages in commercial PVC film rather than only bioamine sensing in tube. Satisfactory accuracy (98.5%) by using DCNN technique indicates the feasibility of the system integration with food supply chains. Furthermore, by utilizing materials with different gas responsive ability, our system can recognize other volatile flavor components such as ethylene, aldehydes, polyphenols and sulfides, which could provide a platform for food quality control or species identification.

In summary, we combined cross-reactive colorimetric barcodes with DCNN to build a simple platform for rapid, non-destructive monitoring of meat freshness in real time via a smartphone APP interface. Like the mammalian olfactory system, our cross-reactive colorimetric barcode detected gases released by rotting meats and formed a scent fingerprint. We used DCNN to identify this fingerprint, allowing the meats to be rapidly categorized as either fresh, less fresh, or spoiled with an overall prediction accuracy of 98.5%. This accuracy is much higher than the commonly used ED analysis (61.7% overall accuracy). Unlike TVB-N measurements (the current gold standard for measuring meat freshness), our technology is non-destructive, automated and enables real-time monitoring. Because the colorimetric barcode can be easily mass-produced and the components are biodegradable and non-toxic, we expect this system to be widely used in the food industry and by the public. It offers consumers and all stakeholders in the food supply chain a way to monitor and/or screen food freshness and establish public confidence.

Supporting Information

Supporting Information is available from the Wiley Online Library or from the author.

Acknowledgements

L.G. and T.W. contributed equally to this work. The authors thank the financial support from the Agency for Science, Technology and Research (A*STAR) under its AME Programmatic Funding Scheme (Project #A18A1b0045), the National Research Foundation (NRF), Prime Minister's office, Singapore, under its NRF Investigatorship (NRF-NRF12017-07), Singapore Ministry of Education (MOE2017-T2-2-107), Accelerating Creativity and Excellence (ACE) awards of NTU, and the funding of China Scholarship Council (CSC). The authors thank Dr. Ai Lin Chun for critical reading and editing of the manuscript.

Conflict of Interest

The authors declare no conflict of interest.

Keywords

colorimetric barcode combinatorics, deep convolutional neural networks, food freshness

Received: July 14, 2020
Revised: August 24, 2020
Published online:

- [1] C. Bushdid, M. O. Magnasco, L. B. Vosshall, A. Keller, *Science* **2014**, *343*, 1370.
- [2] H. Kida, Y. Fukutani, J. D. Mainland, C. A. de March, A. Vihani, Y. R. Li, Q. Chi, A. Toyama, L. Liu, M. Kameda, M. Yohda, H. Matsunami, *Nat. Commun.* **2018**, *9*, 4556.
- [3] T. Pluskal, J.-K. Weng, *Chem. Soc. Rev.* **2018**, *47*, 1592.
- [4] A. Joseph, G. C. DeLuca, *J. Neurol. Neurosurg. Psychiatry* **2016**, *87*, 1146.
- [5] M. E. Berck, A. Khandelwal, L. Claus, L. Hernandez-Nunez, G. Si, C. J. Tabone, F. Li, J. W. Truman, R. D. Fetter, M. Louis, *Elife* **2016**, *5*, 347.
- [6] N. Imam, T. A. Cleland, *Nat. Mach. Intell.* **2020**, *2*, 181.
- [7] J. E. Fitzgerald, E. T. H. Bui, N. M. Simon, H. Fenniri, *Trends Biotechnol.* **2017**, *35*, 33.
- [8] W. Hu, L. Wan, Y. Jian, C. Ren, K. Jin, X. Su, X. Bai, H. Haick, M. Yao, W. Wu, *Adv. Mater. Technol.* **2019**, *4*, 1800488.
- [9] T. Wang, M. Wang, L. Yang, Z. Li, X. J. Loh, X. Chen, *Adv. Mater.* **2020**, *32*, 1905522.
- [10] T. Bruderer, T. Gaisl, M. T. Gaugg, N. Nowak, B. Streckenbach, S. Müller, A. Moeller, M. Kohler, R. Zenobi, *Chem. Rev.* **2019**, *119*, 10803.
- [11] M. Struzik, I. Garbayo, R. Pfenninger, J. L. M. Rupp, *Adv. Mater.* **2018**, *30*, 1804098.
- [12] T. Wang, Y. Guo, P. Wan, X. Sun, H. Zhang, Z. Yu, X. Chen, *Nanoscale* **2017**, *9*, 869.
- [13] Y. Geng, M. A. Ali, A. J. Clulow, S. Fan, P. L. Burn, I. R. Gentle, P. Meredith, P. E. Shaw, *Nat. Commun.* **2015**, *6*, 8240.
- [14] R. Jia, W. Tian, H. Bai, J. Zhang, S. Wang, J. Zhang, *Nat. Commun.* **2019**, *10*, 795.
- [15] G. Barandun, M. Soprani, S. Naficy, M. Grell, M. Kasimatis, K. L. Chiu, A. Ponzoni, F. Güder, *ACS Sens.* **2019**, *4*, 1662.
- [16] M. B. Banerjee, R. B. Roy, B. Tudu, R. Bandyopadhyay, N. Bhattacharyya, *J. Food Eng.* **2019**, *244*, 55.
- [17] J. C. Machado, F. M. Shimizu, M. Ortiz, M. S. Pinhatti, O. Carr, S. S. Guterres, O. N. Oliveira Jr, N. M. Volpato, *Bull. Chem. Soc. Jpn.* **2018**, *91*, 865.
- [18] J. Dai, O. Ogbeide, N. Macadam, Q. Sun, W. Yu, Y. Li, B.-L. Su, T. Hasan, X. Huang, W. Huang, *Chem. Soc. Rev.* **2020**, *49*, 1756.
- [19] J. Chen, Z. Chen, F. Boussaid, D. Zhang, X. Pan, H. Zhao, A. Bermak, C.-Y. Tsui, X. Wang, Z. Fan, *ACS Nano* **2018**, *12*, 6079.
- [20] M. J. Kangas, R. M. Burks, J. Atwater, R. M. Lukowicz, A. E. Holmes, *Crit. Rev. Anal. Chem.* **2016**, *47*, 138.
- [21] Z. Li, K. S. Suslick, *Angew. Chem., Int. Ed.* **2019**, *58*, 14193.
- [22] N. A. Rakow, K. S. Suslick, *Nature* **2000**, *406*, 710.
- [23] M. K. LaGasse, K. McCormick, Z. Li, H. Khanjian, M. Schilling, K. S. Suslick, *J. Am. Inst. Conserv.* **2018**, *57*, 127.
- [24] Z. Li, J. R. Askim, K. S. Suslick, *Chem. Rev.* **2019**, *119*, 231.
- [25] I. Kiselev, V. Sysoev, I. Kaikov, I. Koroncz, R. A. A. Tegin, J. Smanaliev, M. Sommer, C. Ilicali, M. Hauptmann, *Sensors* **2018**, *18*, 550.
- [26] Z. Li, M. Fang, M. K. LaGasse, J. R. Askim, K. S. Suslick, *Angew. Chem., Int. Ed.* **2017**, *56*, 9860.
- [27] K. Divya, M. S. Jisha, *Environ. Chem. Lett.* **2018**, *16*, 101.
- [28] Z. Cao, X. Luo, Z. Hao, F. Zhen, F. Yu, *Cellulose* **2016**, *23*, 1349.

- [29] W. Chen, H. Yu, S.-Y. Lee, T. Wei, J. Li, Z. Fan, *Chem. Soc. Rev.* **2018**, 47, 2837.
- [30] E. Schoolaert, R. Hoogenboom, K. D. Clerck, *Adv. Funct. Mater.* **2017**, 27, 1702646.
- [31] D. Doeun, M. Davaatseren, M.-S. Chung, *Food. Sci. Biotechnol.* **2017**, 26, 1463.
- [32] V. R. Heerthana, R. Preetha, *Rev. Aquacult.* **2019**, 11, 220.
- [33] D. Gibert, C. Mateu, J. Planes, in *Int. Conf. on Artificial Neural Networks*, Springer, Cham, Switzerland **2018**, pp. 383–391.
- [34] K. Nguyen, C. Fookes, S. Sridharan, in *IEEE Winter Conf. on Applications of Computer Vision (WACV)*, IEEE, Piscataway, NJ, USA **2017**.
- [35] L. Liu, A. Rahimpour, A. Taalimi, H. Qi, in *IEEE Int. Conf. on Image Processing (ICIP)*, IEEE, Piscataway, NJ, USA **2017**.
- [36] M. Wang, T. Wang, P. Cai, X. Chen, *Small Methods* **2019**, 3, 1900025.
- [37] A. Esteva, B. Kuprel, R. A. Novoa, J. Ko, S. M. Swetter, H. M. Blau, S. Thrun, *Nature* **2017**, 542, 115.
- [38] Y. Gurovich, Y. Hanani, O. Bar, G. Nadav, N. Fleischer, D. Gelbman, L. Basel-Salmon, P. M. Krawitz, S. B. Kamphausen, M. Zenker, L. M. Bird, K. W. Gripp, *Nat. Med.* **2019**, 25, 60.
- [39] M. Wang, Z. Yan, T. Wang, P. Cai, S. Gao, Y. Zeng, C. Wan, H. Wang, L. Pan, J. Yu, S. Pan, K. He, J. Lu, X. Chen, *Nat. Electron.* **2020**, 3, 563.
- [40] L.-Y. Chang, M.-Y. Chuang, H.-W. Zan, H.-F. Meng, C.-J. Lu, P.-H. Yeh, J.-N. Chen, *ACS Sens.* **2017**, 2, 531.
- [41] H. Lee, M. S. Kim, W.-H. Lee, B.-K. Cho, *Sens. Actuators, B* **2018**, 259, 532.
- [42] C. Rukchon, A. Nopwinyuwong, S. Trevanich, T. Jinkarn, P. Suppakul, *Talanta* **2014**, 130, 547.
- [43] J.-S. Byun, J. S. Min, I. S. Kim, J.-W. Kim, M.-S. Chung, M. Lee, *J. Food Prot.* **2003**, 66, 1733.
- [44] K. He, X. Zhang, S. Ren, S. Jian, in *IEEE Conf. on Computer Vision & Pattern Recognition*, IEEE, Piscataway, NJ, USA **2016**.
- [45] M. Zhong, C. Ping, C. Wen, Y. Kun, P. Lijia, S. Yi, Y. Guihua, *Nano Lett.* **2018**, 18, 4570.
- [46] S. F. Liu, A. R. Petty, G. T. Sazama, T. M. Swager, *Angew. Chem., Int. Ed.* **2015**, 54, 6554.
- [47] Q. Liu, N. Zhao, D. Zhou, Y. Sun, K. Sun, L. Pan, K. Tu, *Food Chem.* **2018**, 262, 226.
- [48] H. Liu, Q. Li, B. Yan, L. Zhang, Y. Gu, *Sensors* **2018**, 19, 45.
- [49] S. Grassi, S. Benedetti, M. Opizzio, E. d. Nardo, S. Buratti, *Sensors* **2019**, 19, 3225.
- [50] T. Liu, W. Zhang, M. Yuwono, M. Zhang, M. Ueland, S. L. Forbes, S. W. Su, *Sens. Actuators, B* **2020**, 311, 127868.
- [51] Z. Li, K. S. Suslick, *ACS Sens.* **2016**, 1, 1330.
- [52] X. Zhong, D. Huo, H. Fa, X. Luo, Y. Wang, Y. Zhao, C. Hou, *Sens. Actuators, B* **2018**, 274, 464.
- [53] V. Y. Musatov, V. V. Sysoev, M. Sommer, I. Kiselev, *Sens. Actuators, B* **2010**, 144, 99.